# Mesoporous Monoclinic CaIn$_2$S$_4$ with Surface Nanostructure: An Efficient Photocatalyst for Hydrogen Production under Visible Light

Jianjun Ding,*[†,‡] Bin Hong,[†,‡] Zhenlin Luo,[†,‡] Song Sun,[†,‡] Jun Bao,*[†,‡] and Chen Gao[†,‡]

[†]National Synchrotron Radiation Laboratory and Collaborative Innovation Center of Chemistry for Energy Materials, University of Science and Technology of China, Hefei, Anhui 230029, China

[‡]CAS Key Laboratory of Materials for Energy Conversion, Department of Materials Science and Engineering, University of Science and Technology of China, Hefei, Anhui 230026, China

Ⓢ *Supporting Information*

ABSTRACT: A novel ternary sulfide photocatalyst of monoclinic CaIn$_2$S$_4$ with excellent photocatalytic H$_2$ evolution activity is synthesized via a high-temperature sulfurization approach. The precursor orthorhombic CaIn$_2$O$_4$ can be converted in situ to monoclinic CaIn$_2$S$_4$ by using H$_2$S gas as the sulfurization reagent once the sulfurization temperature exceeds 773 K. The obtained yellow powders have a mesoporous structure and a chain-shape morphology with large surface area and high pore volume. SEM and TEM observations indicate that specific nanostep structures are formed on the surface of monoclinic CaIn$_2$S$_4$. Under visible light irradiation, monoclinic CaIn$_2$S$_4$ exhibits considerable performance for photocatalytic hydrogen production. A high H$_2$ evolution rate of 30.2 μmol/h with good stability is achieved from Na$_2$S/Na$_2$SO$_3$ aqueous solution with the deposition of 0.5 wt % Pt nanoparticles, 30 times higher than that of cubic CaIn$_2$S$_4$, which makes it a new promising candidate photocatalyst for hydrogen production. This work can provide an effective approach to the fabrication of other mesoporous sulfide photocatalysts with high performance.
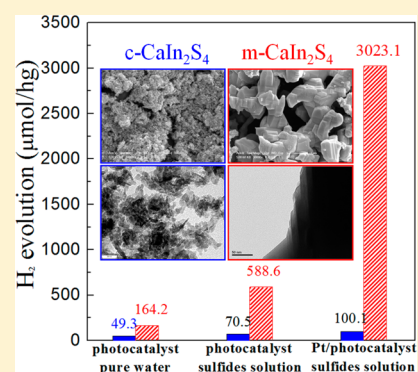
■ INTRODUCTION

The development of visible-light-driven photocatalysts with high performance is of great importance for its potential application in solar energy conversion and environmental purification since visible light represents about 43% of the total radiation emitted by the sun. In past decades, numerous efforts are devoted to the development of new materials with intrinsic visible photocatalytic activities, such as metal oxides,[1,2] metal sulfides/oxysulfides,[3,4] metal nitrides/oxynitrides,[5,6] and metal-free photocatalysts.[7,8] Among the sulfides studied, ternary metal sulfides, such as ZnIn$_2$S$_4$[9−11] and CdIn$_2$S$_4$,[12,13] are promising candidates for their suitable band gaps, good photocatalytic performance, and high stability. In our previous studies, cubic CaIn$_2$S$_4$ and CaIn$_2$S$_4$-reduced graphene oxide nanocomposites were successfully synthesized for applications in hydrogen production and the degradation of organic pollutants under visible light, respectively.[14,15]

Mesoporous material with high surface area and large pore volume exhibits the obvious advantages for photocatalytic application because it can provide more adsorption and reaction sites during the photocatalytic reaction. Until now, most of the related studies have been focused on the synthesis of mesoporous metal oxides, such as TiO$_2$,[16,17] WO$_3$,[18,19] etc. Recently, a few efforts have also been carried out on the development of mesoporous metal sulfides.[20,21] The template-based technique is considered as the main method to prepare mesoporous metal sulfides. However, the removal of templates either by solvent extraction or by high-temperature annealing may not be helpful because of the collapse of the mesoporous framework. Therefore, it is a great challenge to find suitable synthetic method for the fabrication of mesoporous metal sulfides with high quality for the better understanding on their photocatalytic performance.

The high-temperature reductive sulfurization approach has been proved to be an effective method for the fabrication of metal sulfides/oxysulfides, such as CdS,[22] WS$_2$,[23] (AgIn)$_x$Zn$_{2(1−x)}$S$_2$,[24] and Sm$_2$Ti$_2$S$_2$O$_5$.[25] In this study, we report for the first time the design and synthesis of a novel mesoporous ternary metal sulfide with excellent visible-light-driven photocatalytic H$_2$ activity using the high-temperature sulfurization approach. Hydrogen sulfide (H$_2$S) gas was used as the sulfurization reagent, and the metal precursor was orthorhombic CaIn$_2$O$_4$ which was prepared according to our previous study.[26] The metal precursor can be converted to monoclinic CaIn$_2$S$_4$ (m-CaIn$_2$S$_4$) crystallites once the sulfurization temperature exceeds 773 K. H$_2$S gas molecules can easily diffuse and transport in the prime mesopore channels. The obtained yellow products have a mesoporous structure and a chain-like morphology with high surface area (86−109 m^2/g) and large pore volume (0.118−0.145 cm^3/g). Specific nanostep structures can be formed on the surface of m-CaIn$_2$S$_4$ particles after the sulfurization process. As a result, m-CaIn$_2$S$_4$ shows

excellent hydrogen evolution activity under visible light ($\lambda >$ 420 nm) irradiation with a maximum H_2 evolution rate of 30.2 μmol/h, which is about 30 times higher than that of cubic $CaIn_2S_4$ (c-$CaIn_2S_4$) reported previously.[14] This work may provide some useful information about the preparation of other mesoporous sulfide photocatalysts, especially ternary metal sulfides, with efficient performance in the field of solar energy conversion.

■ EXPERIMENTAL SECTION

Photocatalyst Preparation. Indium nitrate and chloroplatinic acid were purchased from Aladdin Industrial Inc. Calcium nitrate, thiacetamide, and glycine were supplied by Sinopharm Chemical Reagent Co., Ltd. All other reagents were at least of analytical reagent grade and used without further purification. Deionized (DI) water was used in all experiments.

Orthorhombic $CaIn_2O_4$ rods were prepared using a solution combustion method followed by a high-temperature post-annealing according to our previous study.[26] Monoclinic $CaIn_2S_4$ (m-$CaIn_2S_4$) was synthesized from the oxide precursor $CaIn_2O_4$ (1.0 g) by calcination under flowing H_2S (10% H_2S/ 90% N_2, flow rate 50 mL/min) at different temperatures (673– 1073 K) for different times (3–12 h). After the sulfurization process, the color of the powder was changed from white to yellow.

In control synthesis experiments, cubic $CaIn_2S_4$ (c-$CaIn_2S_4$) was obtained using a hydrothermal method according to our previous work.[14] Simply, a given amount of metal nitrates and thiacetamide was dissolved in DI water and then hydrothermally synthesized at 433 K for 16 h. After washing and drying, the powder was annealing at 873 K for 3 h in pure Ar to improve the crystallinity.

In order to improve the photocatalytic H_2 evolution activity, the Pt nanoparticles were used as the cocatalyst to modify m-$CaIn_2S_4$ and c-$CaIn_2S_4$ by an incipient impregnation method. The dry powder was impregnated with an aqueous solution of chloroplatinic acid. To achieve incipient wetness, a liquid/solid ratio of 1.75 and 0.24 cm^3/g was used respectively for m-$CaIn_2S_4$ and c-$CaIn_2S_4$. After impregnation, the sample was dried at 383 K for 24 h and then reduced at 573 K in pure H_2 for 2 h. In addition, a Pt(0.5 wt %)/m-$CaIn_2S_4$ was also fabricated by a photoreduction method from an aqueous solution of $H_2PtCl_6\cdot6H_2O$ (Aladdin, Pt $\geq$ 37.5%).

The m-$CaIn_2S_4$ and c-$CaIn_2S_4$ electrodes were fabricated using a simple dip-coating method. At first, 20 mg of photocatalyst was suspended in 50 mL of absolute ethanol by ultrasonication to get a suspension. Then, the suspension was dip-coated onto a 1 cm × 2 cm ITO glass electrode placed on a 343 K heating station. After the elimination of ethanol, the dip-coating process was repeated ten times to obtain the final electrodes.

Photocatalytic Experiments. The photocatalytic activity for water splitting was measured in a 330 mL top-irradiation gas-closed circulation reactor. Photoirradiation was carried out using a 300 W Xe arc lamp (PLS-SXE 300, ChangTuo Ltd.) through infrared and UV cutoff filters to ensure visible illumination only (420 nm $\leq \lambda \leq$ 750 nm). The distance between the lamp and the solution surface was 30 cm.

In a typical photocatalytic experiment, 10 mg of the photocatalyst was added into the reactor with constant stirring in a 100 mL of DI water or Na_2S/Na_2SO_3 solution (0.025 M). To eliminate any thermal effect, a water jacket outside the reactor was used to keep the solution temperature constant at

room temperature by flowing cooling water. Before the reaction, the circulation system was purged with argon several times to remove the dissolved oxygen. A 0.5 mL sample of the generated gas was collected intermittently through the septum using a SGE syringe, and hydrogen content was analyzed by a gas chromatograph (Shimadzu GC 14C, TCD, argon as a carrier gas, equipped with a TDX01 column).

Characterization. Powder X-ray diffraction (XRD) patterns were measured using a Rigaku TTR III diffractometer with Cu Kα radiation (λ = 0.154 18 nm) at a scan rate of 5° min^{-1} to determine the crystal phase of the prepared samples. The morphology and microstructure of the samples were investigated by a scanning electron microscope (Sirion 200) and a transmission electron microscope (JEM-2100F). Nitrogen adsorption−desorption isotherms were recorded on a Micromeritics ASAP 2020 M+C accelerated surface area and porosimetry system at 77 K. The surface areas were estimated using the Brunauer−Emmett−Teller (BET) method. The UV/ vis diffuse reflectance spectrum of photocatalysts was measured at room temperature using a UV/vis spectrometer (SolidSpec-3700, Shimadzu, Japan). The surface characterization was carried out using an X-ray photoelectron spectroscope (XPS, ESCALAB 250, Thermo-VG Scientific) with a base pressure lower than 1.0×10^{-10} Pa and Mg Kα radiation (E = 1253.6 eV) operated at 150 W as the X-ray source. The elemental composition of the photocatalyst was determined by inductively coupled plasma atomic emission spectrometry (ICP-AES, Optima 7300 DV, PerkinElmer Corporation), X-ray fluorescence (XRF, Shimadzu, VF-320), and a VarioELIII instrument. The photoelectrochemical properties were measured on a CHI-760D electrochemical analyzer in a standard three-electrode system using the prepared samples with an active area of ca. 1 cm^2 as the working electrodes, a platinum wire as the counter electrode, and Ag/AgCl as the reference electrode. KCl (1 M, pH = 7) solution was used as the electrolyte.

■ RESULTS AND DISCUSSION

Structure and Morphology Characterizations. The chemical compositions of the as-prepared m-$CaIn_2S_4$ (873 K/ 9 h, the highest H_2 evolution activity) were accurately determined by ICP-AES and XRF, as shown in Table S1. Overall, the compositions analyzed using ICP-AES and XRF were similar to each other, within 4%, which means relatively good reproducibility. The average ratio of Ca/In and Ca/S was 0.4985 and 0.2465, respectively. The chemical composition of the as-synthesized sample was calculated to be $CaIn_{2.01}S_{4.06}$. The yield of the final product was also measured. After being sulfurized at 873 K for 9 h, 1.000 g of $CaIn_2O_4$ was converted to 1.207 g of powder, which indicates that almost all the oxygen atoms have been displaced by the sulfur atoms. For convenience, the sample is still written as m-$CaIn_2S_4$.

To further investigate the surface compositions and chemical states of the as-prepared m-$CaIn_2S_4$, XPS measurements were carried out. The typical survey spectrum and high-resolution element spectra of m-$CaIn_2S_4$ (873 K/9 h) are shown in Figure 1. It reveals that no peaks of other elements except Ca, In, S, O, and C were observed. The peaks of O and C probably come from H_2O, O_2, and CO_2 absorbed on the surface of the sample before characterization and adventitious hydrocarbon from XPS instrument itself.[27] Characteristic binding energies of 346.6 and 350.2 eV for Ca^{2+} 2p, 443.8 and 451.3 eV for In^{3+} 3d, and 161.6 and 162.7 eV for S^{2-} 2p are observed for m-$CaIn_2S_4$. These
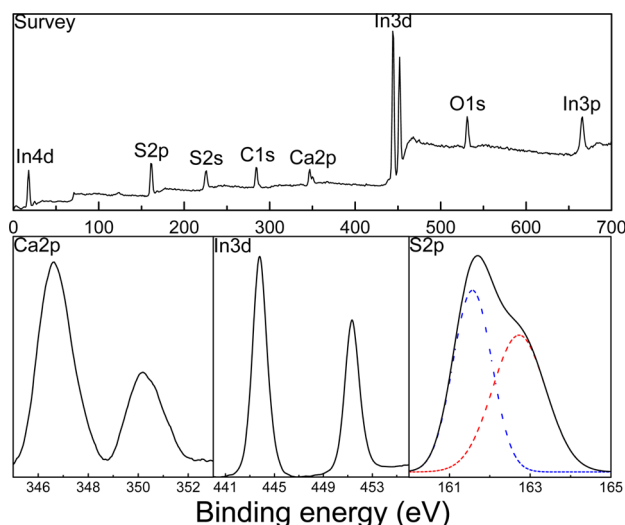
Figure 1. XPS spectra of m-CaIn$_2$S$_4$.

results indicate the oxidation states of element Ca, In, and S are +2, +3, and −2, respectively.[28,29]

Figure 2 shows the XRD patterns of precursor CaIn$_2$O$_4$ and m-CaIn$_2$S$_4$. For precursor CaIn$_2$O$_4$, all the peaks can be well
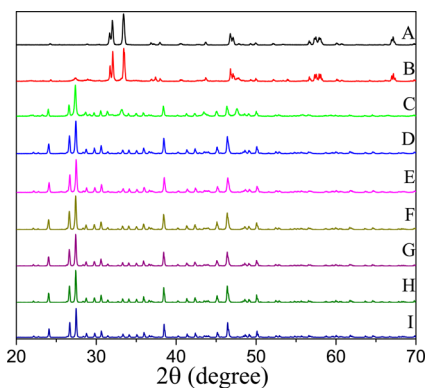

Figure 2. XRD patterns of precursor CaIn$_2$O$_4$ (A) and m-CaIn$_2$S$_4$ sulfurized in different temperatures and times: (B) 673 K/9 h; (C) 773 K/9 h; (D) 873 K/9 h; (E) 973 K/9 h; (F) 1073 K/9 h; (G) 873 K/3 h; (H) 873 K/6 h; (I) 873 K/12 h.

indexed to the orthorhombic phase (Figure 2A, PDF #17-0643). When sulfurization temperature was lower than 873 K (Figure 2B,C), there remains a certain amount of CaIn$_2$O$_4$, indicating the incomplete phase evolution. Complete sulfurization of the CaIn$_2$O$_4$ precursor can be achieved once the temperature reached 873 K. As shown in Figure 2D−F, there was no obvious difference in XRD patterns in terms of XRD peak position and intensity by changing the sulfurization temperature from 873 to 1073 K for 9 h or by changing the sulfurization time from 3 to 12 h at 873 K. No peaks attributable to CaIn$_2$O$_4$ or other sulfides are found, and all the peaks can be indexed to the phase of monoclinic Ca$_{3.1}$In$_{6.6}$S$_{13}$ (namely CaIn$_{2.13}$S$_{4.19}$, PCPDF #72-0875). The results show that the pure phase of m-CaIn$_2$S$_4$ with good crystallinity can be obtained, and no other impurities are found when the sulfurization temperature reaches 873 K. Although the XRD patterns are in accordance with that of Ca$_{3.1}$In$_{6.6}$S$_{13}$, there are some apparent differences in the values of composition. The reason may be explained by the difference of synthesis method

and analysis technique. The compound Ca$_{3.1}$In$_{6.6}$S$_{13}$ was prepared by chemical transport reactions with iodine in the gas phase, and the composition was analyzed using the quantitative electron microprobe analysis,[30] while m-CaIn$_2$S$_4$ was synthesized via sulfurization of pure CaIn$_2$O$_4$ under H$_2$S flow and the composition was determined using ICP-AES and XRF. For contrast, c-CaIn$_2$S$_4$ was also prepared using the hydrothermal method, and the XRD pattern was consistent with the cubic structure of CaIn$_2$S$_4$ (Figure S1, PDF #31-0272).

Figure 3 shows SEM images of precursor CaIn$_2$O$_4$ and m-CaIn$_2$S$_4$. It can be seen that a large number of rod-shaped
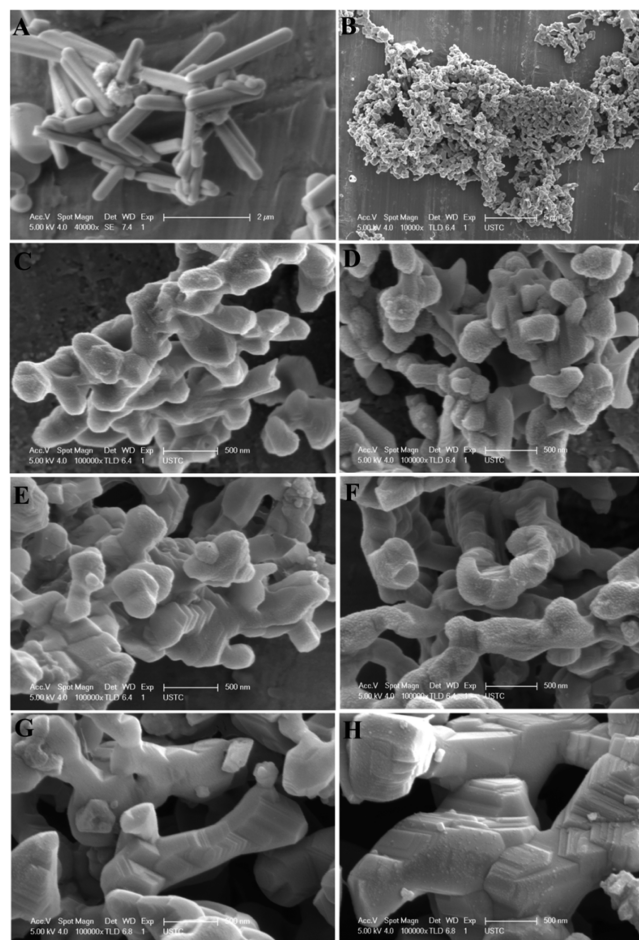

Figure 3. SEM images of precursor CaIn$_2$O$_4$ (A) and m-CaIn$_2$S$_4$ sulfurized in different temperatures and times: (B) 873 K/9 h; (C) 873 K/3 h; (D) 873 K/6 h; (E) 873 K/9 h; (F) 873 K/12 h; (G) 973 K/9 h; (H) 1073 K/9 h.

CaIn$_2$O$_4$ with smooth surface are displayed in Figure 3A. However, after the sulfurization, the rod-shaped morphology was destroyed and a type of chainlike structure was formed. As shown in Figure 3B, these particles linked end-to-end to self-assemble a chain-structure during the sulfurization process, and these m-CaIn$_2$S$_4$ chains are inclined finally to form a net structure with self-agglomerate. From Figure 3C−H, with increasing the sulfurization temperature or time, the average size along the radial direction was increased from 300 to 700 nm (the fine particles on the surface of m-CaIn$_2$S$_4$ were Au nanoparticles for the better observation of SEM characterization). Interestingly, specific nanostep structures were formed on the surface of many particles, which may be self-constructed

during the sulfurization process.[22,24] The quantity of nanosteps increases with increasing the sulfurization temperature or time.

To further study the microscopic morphology of m-CaIn$_2$S$_4$ (873 K/9 h), TEM analysis was performed, as shown in Figure 4. It can be clearly seen that the m-CaIn$_2$S$_4$ particles are linked
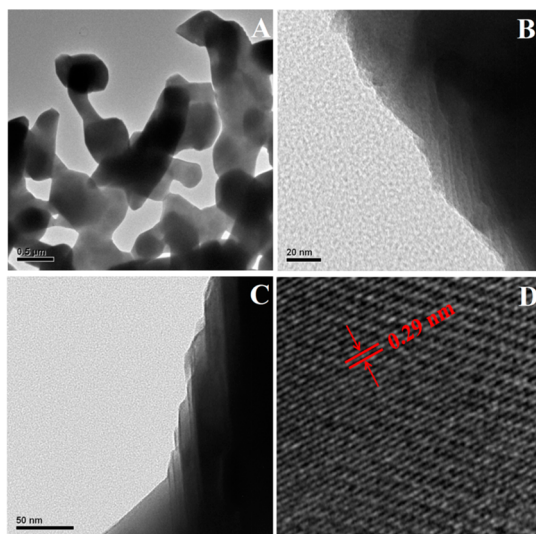

Figure 4. TEM images of m-CaIn$_2$S$_4$ (873 K/9 h).

together (Figure 4A), which is consistent with the results of the SEM measurements. Furthermore, we can also see the existence of the nanostep structure (Figure 4B,C). There are many reports that the nanostep structure can be beneficial for the effective separation of the photogenerated charge carriers during the photocatalytic reaction,[24,31,32] which means it is beneficial to the enhancement of photocatalytic performance. Figure S2 shows a TEM image of a Pt(0.5 wt %)/m-CaIn$_2$S$_4$ fabricated by the photoreduction method. Pt nanoparticles were selectively deposited on the edges of the nanostep structure, which means the photogenerated electrons could readily migrate to the edges of the nanostep structure, and these positions play an important role as reduction sites for hydrogen production. The high-resolution TEM image (Figure 4D) showed the lattice fringes of the m-CaIn$_2$S$_4$ particle, suggesting that the particles were well crystallized. The lattice spacing was measured to be around 0.29 nm, which could be assigned to the (−113) plane of the m-CaIn$_2$S$_4$ crystal structure. The morphology of c-CaIn$_2$S$_4$ was also investigated, as shown in Figure S3. A mixture of differently shaped nanoparticles, including nanorods and nanosheets, was observed.

The BET surface area and porous structure of m-CaIn$_2$S$_4$ (873 K/9 h) were investigated using nitrogen adsorption−desorption experiments, as shown in Figure 5. The sample shows a type IV isotherm with H2 hysteresis loop at a P/P_0 range of 0.2−0.85 according to the IUPAC classification, indicating the existence of ink-bottle-type mesoporous nature. The BET surface area and the pore volume are 102 m^2 g^{-1} and 0.141 cm^3 g^{-1}, respectively. The pore size, obtained from the desorption branch of the isotherms, exhibits a very narrow distribution in the mesopore region between 2 and 4 nm, as shown in the inset of Figure 5. The uniformity of the pore size distribution makes the material with large surface area and high pore volume. An apparent increase in adsorbed volume is observed once the P/P_0 value exceeds 0.85, which may be
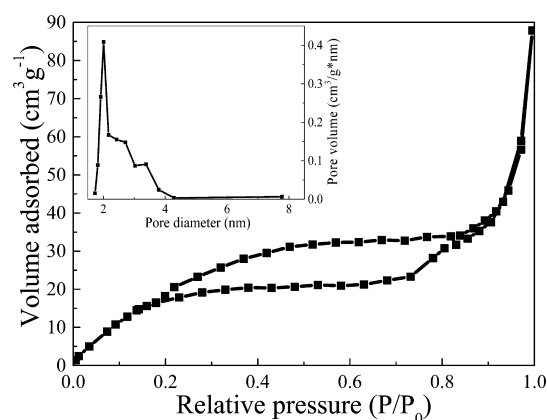

Figure 5. N$_2$ adsorption/desorption isotherm of m-CaIn$_2$S$_4$ (873 K/9 h); the inset is the pore diameter distribution.

caused by the self-agglomerate of chainlike particles (slitlike porosity). A similar phenomenon was reported by Zhao et al. in mesoporous WS2-SBA-15 where WS2 was also prepared using the high-temperature sulfurization approach.[23] The surface area and pore volume of m-CaIn$_2$S$_4$, sulfurized at different temperatures and times, are listed in Table 1. Overall, large surface area (86−109 m^2/g) and high pore volume (0.118−0.145 cm^3/g) of the prepared m-CaIn$_2$S$_4$ are obtained.

Table 1. Surface Area, Pore Volume, Bandgap, and Photocatalytic H$_2$ Evolution Rate of m-CaIn$_2$S$_4$ Sulfurized in Different Temperatures and Times

sample	sulfurization condition	surface area (m^2 g^{-1})	pore volume (cm^3 g^{-1})	bandgap (eV)	H$_2$ rate^a (μmol/h)
1	873 K/3 h	89	0.123	2.40	22.9
2	873 K/6 h	109	0.145	2.44	28.7
3	873 K/9 h	102	0.141	2.62	30.2
4	873 K/12 h	99	0.134	2.76	25.7
5	973 K/9 h	93	0.131	2.78	19.2
6	1073 K/9 h	86	0.118	2.80	13.6

^{a}Photocatalyst: 10 mg; Na$_2$S/Na$_2$SO$_3$: 0.025 M (100 mL); 750 nm ≥ λ ≥ 420 nm.

Figure 6 shows the UV−vis diffuse reflectance absorption spectra of m-CaIn$_2$S$_4$ (873 K/9 h). The strong absorption and
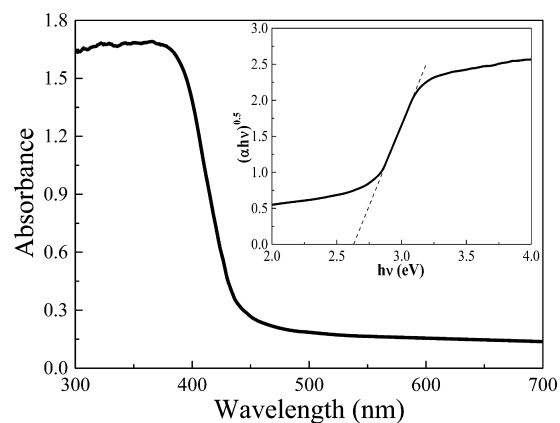

Figure 6. UV−vis diffuse absorption spectrum of m-CaIn$_2$S$_4$ (873 K/9 h); the inset is the plot of transformed Kubelka−Munk function versus the energy of light.

steep absorption edge in the visible region indicate that the absorption relevant to the band gap is due to the band-edge transitions of m-CaIn$_2$S$_4$ rather than the transitions from impurity levels.[33] The absorption cutoff wavelength is about 450 nm, and the band gap was estimated to be 2.62 eV according to the Tauc equation (Figure 6, inset). The value is much higher than that of c-CaIn$_2$S$_4$ (1.76 eV),[14] indicating that the crystal form has an obvious influence on the optical performance and electronic energy band structure. From Table 1, the estimated band gap of m-CaIn$_2$S$_4$ is found to be in the range of 2.40−2.80 eV by changing the sulfurization temperature or time. This is mainly caused by the difference of the grain size.

Photocatalytic Performance. The photocatalytic activity of the as-obtained samples was evaluated from pure water and Na$_2$S/Na$_2$SO$_3$ aqueous solution under visible light irradiation ($\lambda > 420$ nm). Control experiments were carried out in the dark or in the absence of photocatalyst. As there was no appreciable H$_2$ evolution detected, we confirmed that hydrogen was produced by photocatalytic reaction.

The photocatalytic performance for hydrogen evolution over the obtained m-CaIn$_2$S$_4$ is sensitive to the sulfurization temperature and time, as shown in Figure 7A. The result is
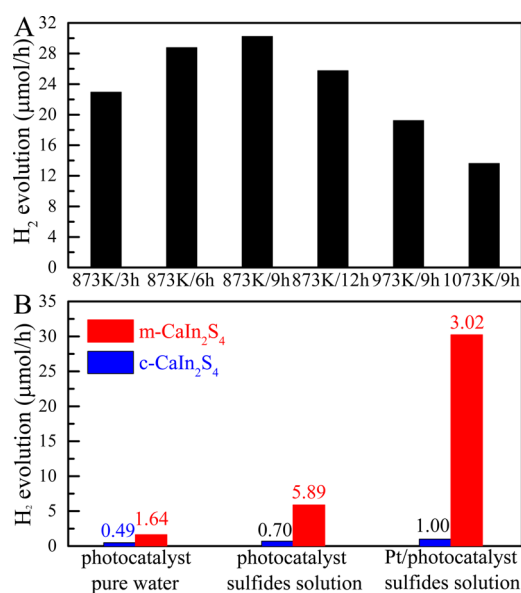

Figure 7. Photocatalytic performance for hydrogen production under visible light irradiation (10 mg of photocatalyst): (A) m-CaIn$_2$S$_4$ sulfurized in different temperatures and times with the deposition of 0.5 wt % Pt nanoparticles; (B) m-CaIn$_2$S$_4$ and c-CaIn$_2$S$_4$ in different experimental conditions.

also listed in Table 1. With the sulfurization time varied from 3 to 12 h at 873 K, the photocatalytic activity of Pt/m-CaIn$_2$S$_4$ experienced an initial improved followed by a rapid decrease. Moreover, reduced activity was observed once the sulfurization temperature exceeds 873 K. The optimal sulfurization condition was found to be 873 K for 9 h. The effect of Pt concentration on the photocatalytic activity over m-CaIn$_2$S$_4$ (873 K/9 h) was also investigated, as shown in Figure S4. The result indicates that a maximum activity was obtained when the concentration of Pt nanoparticles was 0.5 wt %. The presentation below therefore focuses on the sample with the highest activity.

Figure 7B shows the average hydrogen evolution rates of m-CaIn$_2$S$_4$ and c-CaIn$_2$S$_4$ under visible light. In pure water without any sacrificial reagent or cocatalyst, the visible-light-driven photocatalytic H$_2$ evolution rate of m-CaIn$_2$S$_4$ is 1.64 μmol/h, which is about 3.3 times higher than that of c-CaIn$_2$S$_4$ (0.49 μmol/h). When Na$_2$S and Na$_2$SO$_3$ were used as sacrificial reagents, the H$_2$ evolution rate of m-CaIn$_2$S$_4$ and c-CaIn$_2$S$_4$ is increased to 5.89 and 0.70 μmol/h, respectively. In order to further improve the photocatalytic H$_2$ evolution activity, 0.5 wt % Pt nanoparticles as cocatalyst were loaded on the surface of samples to reduce the recombination of photogenerated charges. Interestingly, the amount of hydrogen evolved for Pt0.5/m-CaIn$_2$S$_4$ from Na$_2$S/Na$_2$SO$_3$ aqueous solution is about 30 times higher than that evolved using Pt0.5/c-CaIn$_2$S$_4$. The average hydrogen evolution rate of m-CaIn$_2$S$_4$ was calculated to be 30.2 μmol/h (3.02 mmol h^{-1} g^{-1}). This indicates that m-CaIn$_2$S$_4$ showed excellent activity for photocatalytic hydrogen evolution than c-CaIn$_2$S$_4$ under visible light irradiation.

To evaluate the photocatalytic and chemical stability for practical applications, the recycling experiments show that no obvious decrease of H$_2$ evolution was observed for m-CaIn$_2$S$_4$ (873 K/9 h) after four cycling runs of 24 h either from pure water or Na$_2$S/Na$_2$SO$_3$ aqueous solution with the deposition of Pt, as shown in Figure 8 and Figure S5. At the same time, there
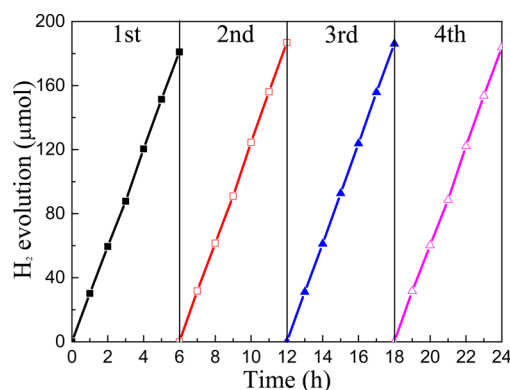

Figure 8. Stability of photocatalytic H$_2$ evolution for Pt0.5/m-CaIn$_2$S$_4$ (873 K/9 h) from Na$_2$S/Na$_2$SO$_3$ aqueous solution under visible light irradiation.

was no appreciable difference in XRD patterns, XPS spectra, and TEM image of the photocatalyst before and after the reaction (Figures S6 and S7). It should be noted that the deposition of Pt via hydrogen reduction at 673 K for 2 h did not change the crystal structure of m-CaIn$_2$S$_4$. All these results suggest that the high photocatalytic activity and good stability of the m-CaIn$_2$S$_4$ photocatalyst.

It has been established that the m-CaIn$_2$S$_4$ sample which has lower ability to absorb visible light exhibits much higher photocatalytic activity for hydrogen production than c-CaIn$_2$S$_4$ under similar conditions. The results of our present work raise a question why m-CaIn$_2$S$_4$ and c-CaIn$_2$S$_4$ show such a significant difference in their photocatalytic activities for hydrogen production. As we known, photocatalysts with different crystal forms may differ in morphology, electronic energy band structure, and their photocatalytic activities, such as TiO$_2$ (anatase, rutile and brookite),[34] In$_2$S$_3$ (tetragonal and cubic),[35] BiVO$_4$ (monoclinic and tetragonal),[36] etc. Here, the excellent performance of m-CaIn$_2$S$_4$ can be ascribed to large surface area/pore volume, high separation efficiency of

photogenerated charge carriers, and more negative conduction-band potential.

First, the nanostep structure on the surface of m-$CaIn_2S_4$ could be beneficial for effective separation of the photo-generated charges according to previous studies.[24,31,32] Figure 9
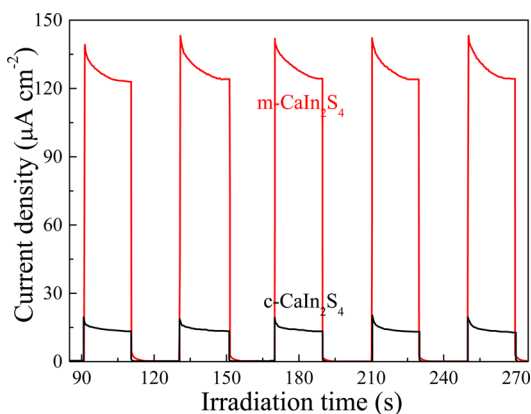

Figure 9. Transient photocurrent density responses of m-$CaIn_2S_4$ and c-$CaIn_2S_4$ at a potential bias of 0.2 V (vs Ag/AgCl).

shows the photocurrent–time curves under visible-light irradiation. The photocurrent density of m-$CaIn_2S_4$ (873 K/9 h) is about 8 times higher than that of c-$CaIn_2S_4$. It is known that the photocurrent is formed mainly by the diffusion of the photogenerated electrons to the back contact.[37] Therefore, the enhanced photocurrent indicates a more efficient separation of the photogenerated electron–hole pairs in m-$CaIn_2S_4$ compared to c-$CaIn_2S_4$.

Second, as mesoporous m-$CaIn_2S_4$ shows larger surface area and pore volume than c-$CaIn_2S_4$ (6.64 m^2 g^{-1}, 0.037 cm^3 g^{-1}, Figure S8), it can provide more surface active sites for the adsorption of reactant molecules and make the photocatalytic process more efficient.[38,39] The mesoporous structure of m-$CaIn_2S_4$ also contributes to reduce the recombination of the bulk electron–hole pairs and improve the separation of the surface electron–hole pairs.[40]

Third, the difference of the electronic band structure between two sulfides is another and important factor. From the valence band XPS spectra (Figure 10), the position of the valence band maximum of m-$CaIn_2S_4$ and c-$CaIn_2S_4$ was calculated to be about 1.30 and 0.88 eV, respectively. Because the band gap of m-$CaIn_2S_4$ and c-$CaIn_2S_4$ is 2.62 and 1.76 eV from the optical absorption spectra, the conduction band
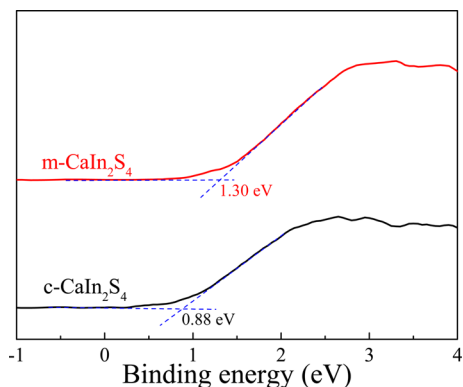
minimum would occur at about at −1.32 and −0.88 eV, respectively, as shown in Figure S9. Further evidence can be obtained from the Mott−Schottky analysis (Figure S10). Reversed sigmoidal plots were observed with an overall shape consistent with that typical for n-type semiconductor. The relative flat-band potential (V_{fb}) of m-$CaIn_2S_4$ and c-$CaIn_2S_4$, calculated from the x-intercept of the linear region, was about −1.2 and −0.98 V (vs NHE, pH7), respectively. As we know, the conduction-band potential of n-type semiconductor is very close (about 0−0.1 V more negative) to the flat-band potential, so it can be deduced that the conduction-band potential of m-$CaIn_2S_4$ is more negative compared to c-$CaIn_2S_4$. Therefore, the reduction capacity of the photogenerated electrons on the conduction band of m-$CaIn_2S_4$ will be higher than that of c-$CaIn_2S_4$.

CONCLUSION

In summary, mesoporous m-$CaIn_2S_4$ with excellent visible-light-driven photocatalytic H_2 evolution activity was successfully synthesized via sulfurization of orthorhombic $CaIn_2O_4$ under H_2S flow. The obtained yellow powders have a mesoporous structure and a chain-shape morphology with large surface area (86−109 m^2/g) and high pore volume (0.118−0.145 cm^3/g). Specific nanostep structures can be formed on the surface of m-$CaIn_2S_4$ particles after the sulfurization process. As a result, m-$CaIn_2S_4$ shows excellent hydrogen evolution activity under visible light (λ > 420 nm) irradiation with a maximum H_2 evolution rate of 30.2 μmol/h, which is about 30 times higher than that of c-$CaIn_2S_4$. The enhanced photocatalytic performance of m-$CaIn_2S_4$ compared to c-$CaIn_2S_4$ can be attributed to large surface area/pore volume, high separation efficiency of photogenerated charge carriers, and more negative conduction-band potential. This work may provide some useful information about the preparation of other mesoporous ternary sulfide photocatalysts with efficient performance.

ASSOCIATED CONTENT

Ⓢ Supporting Information

Chemical compositions of m-$CaIn_2S_4$, XRD pattern, SEM/TEM images and N_2 adsorption−desorption isotherms of cubic $CaIn_2S_4$, TEM images of Pt/m-$CaIn_2S_4$ fabricated by the photoreduction method, photocatalytic performance of Pt/m-$CaIn_2S_4$ as a function of Pt content, stability of photocatalytic H_2 evolution for m-$CaIn_2S_4$ (873 K/9 h) from pure water under visible light irradiation, XRD pattern, XPS spectra and TEM images of m-$CaIn_2S_4$ after photocatalytic reaction, energy band diagram and MS plots of m-$CaIn_2S_4$ and c-$CaIn_2S_4$. This material is available free of charge via the Internet at http://pubs.acs.org.

AUTHOR INFORMATION

Corresponding Authors

*Tel (+86)551-63607492; Fax (+86)551-65141078; e-mail dingjj@ustc.edu.cn (J.D.).
*Tel (+86)551-63607492; Fax (+86)551-65141078; e-mail baoj@ustc.edu.cn (J.B.).

Notes

Figure 10. VB XPS spectra for m-$CaIn_2S_4$ and c-$CaIn_2S_4$.

ACKNOWLEDGMENTS

REFERENCES

(1) Zhang, C.; Zhu, Y. Synthesis of Square Bi_2WO_6 Nanoplates as High-Activity Visible-Light-Driven Photocatalysts. *Chem. Mater.* **2005**, *17*, 3537−3545.

(2) Yi, Z.; Ye, J.; Kikugawa, N.; Kato, T.; Ouyang, S.; Stuart-Williams, H.; Yang, H.; Cao, J.; Luo, W.; Li, Z.; et al. An Orthophosphate Semiconductor with Photooxidation Properties under Visible-Light Irradiation. *Nat. Mater.* **2010**, *9*, 559−564.

(3) Bao, N.; Shen, L.; Takata, T.; Domen, K. Self-Templated Synthesis of Nanoporous CdS Nanostructures for Highly Efficient Photocatalytic Hydrogen Production under Visible Light. *Chem. Mater.* **2008**, *20*, 110−117.

(4) Ishikawa, A.; Takata, T.; Kondo, J.; Hara, M.; Kobayashi, H.; Domen, K. Oxysulfide $Sm_2Ti_2S_2O_5$ as a Stable Photocatalyst for Water Oxidation and Reduction under Visible Light Irradiation ($\lambda \leq 650$ nm). *J. Am. Chem. Soc.* **2002**, *124*, 13547−13553.

(5) Hitoki, G.; Ishikawa, A.; Takata, T.; Kondo, J.; Hara, M.; Domen, K. Ta_3N_5 as a Novel Visible Light Driven Photocatalyst ($\lambda < 600$ nm). *Chem. Lett.* **2002**, *31*, 736−737.

(6) Maeda, K.; Teramura, K.; Lu, D.; Takata, T.; Saito, N.; Inoue, Y.; Domen, K. Photocatalyst Releasing Hydrogen from Water. *Nature* **2006**, *440*, 295.

(7) Wang, X.; Maeda, K.; Thomas, A.; Takanabe, K.; Xin, G.; Carlsson, J.; Domen, K.; Antonietti, M. A Metal-Free Polymeric Photocatalyst for Hydrogen Production from Water under Visible Light. *Nat. Mater.* **2009**, *8*, 76−80.

(8) Yeh, T.; Syu, J.; Cheng, C.; Chang, T.; Teng, H. Graphite Oxide as a Photocatalyst for Hydrogen Production from Water. *Adv. Funct. Mater.* **2010**, *20*, 2255−2262.

(9) Lei, Z.; You, W.; Liu, M.; Zhou, G.; Takata, T.; Hara, M.; Domen, K.; Li, C. Photocatalytic Water Reduction under Visible Light on a Novel $ZnIn_2S_4$ Catalyst Synthesized by Hydrothermal Method. *Chem. Commun.* **2003**, *17*, 2142−2143.

(10) Shen, S.; Zhao, L.; Guo, L. Cetyltrimethylammonium bromide (CTAB)-Assisted Hydrothermal Synthesis of $ZnIn_2S_4$ as an Efficient Visible-Light-Driven Photocatalyst for Hydrogen Production. *Int. J. Hydrogen Energy* **2008**, *33*, 4501−4510.

(11) Zhou, J.; Tian, G.; Chen, Y.; Meng, X.; Shi, Y.; Cao, X.; Pan, K.; Fu, H. In Situ Controlled Growth of $ZnIn_2S_4$ Nanosheets on Reduced Graphene Oxide for Enhanced Photocatalytic Hydrogen Production Performance. *Chem. Commun.* **2013**, *49*, 2237−2239.

(12) Kale, B.; Baeg, J.; Lee, S.; Chang, H.; Moon, S.; Lee, C. $CdIn_2S_4$ Nanotubes and "Marigold" Nanostructures: A Visible-Light Photocatalyst. *Adv. Funct. Mater.* **2006**, *16*, 1349−1354.

(13) Bhirud, A.; Chaudhari, N.; Nikam, L.; Sonawane, R.; Patil, K.; Baeg, J.; Kale, B. Surfactant Tunable Hierarchical Nanostructures of $CdIn_2S_4$ and Their Photohydrogen Production under Solar Light. *Int. J. Hydrogen Energy* **2011**, *36*, 11628−11639.

(14) Ding, J.; Sun, S.; Yan, W.; Bao, J.; Gao, C. Photocatalytic H_2 Evolution on a Novel $CaIn_2S_4$ Photocatalyst under Visible Light Irradiation. *Int. J. Hydrogen Energy* **2013**, *38*, 13153−13158.

(15) Ding, J.; Yan, W.; Sun, S.; Bao, J.; Gao, C. Hydrothermal Synthesis of $CaIn_2S_4$-Reduced Graphene Oxide Nanocomposites with Increased Photocatalytic Performance. *ACS Appl. Mater. Interfaces* **2014**, *6*, 12877−12884.

(16) Joo, J.; Lee, I.; Dahl, M.; Moon, G.; Zaera, F.; Yin, Y. Controlled Synthesis of Mesoporous TiO_2 Hollow Shells: Toward an Efficient Photocatalyst. *Adv. Funct. Mater.* **2013**, *23*, 4246−4254.

(17) Qiu, B.; Xing, M.; Zhang, J. Mesoporous TiO_2 Nanocrystals Growth in Situ on Graphene Aerogels for High Photocatalysis and Lithium-Ion Batteries. *J. Am. Chem. Soc.* **2014**, *136*, 5852−5855.

(18) Santato, C.; Odziemkowshi, M.; Ulmann, M.; Augustynski, J. Crystallographically Oriented Mesoporous WO_3 Film: Synthesis, Characterization, and Applications. *J. Am. Chem. Soc.* **2001**, *123*, 10639−10649.

(19) Huang, H.; Yue, Z.; Li, G.; Wang, X.; Huang, J.; Du, Y.; Yang, P. Ultraviolet-Assisted Preparation of Mesoporous WO_3/Reduced Graphene Oxide Composites: Superior Interfacial Contacts and Enhanced Photocatalysis. *J. Mater. Chem. A* **2013**, *1*, 15110−15116.

(20) Braun, P.; Osenar, P.; Tohver, V.; Kennedy, S.; Stupp, S. Nanostructure Templating in Inorganic Solids with Organic Lyotropic Liquid Crystals. *J. Am. Chem. Soc.* **1999**, *121*, 7302−7309.

(21) Gao, F.; Lu, Q.; Zhao, D. Synthesis of Crystalline Mesoporous CdS Semiconductor Nanoarrays Through a Mesoporous SBA-15 Silica Template Technique. *Adv. Mater.* **2003**, *15*, 739−742.

(22) Jing, D.; Guo, L. A Novel Method for the Preparation of a Highly Stable and Active CdS Photocatalyst with a Special Surface Nanostructure. *J. Phys. Chem. B* **2006**, *110*, 11139−11145.

(23) Shi, Y.; Wan, Y.; Liu, R.; Tu, B.; Zhao, D. Synthesis of Highly Ordered Mesoporous Crystalline WS_2 and MoS_2 *via* a High-Temperature Reductive Sulfuration Route. *J. Am. Chem. Soc.* **2007**, *129*, 9522−9531.

(24) Tsuji, I.; Kato, H.; Kobayashi, H.; Kudo, A. Photocatalytic H_2 Evolution Reaction from Aqueous Solutions over Band Structure-Controlled $(AgIn)_xZn_{(1-x)}S_2$ Solid Solution Photocatalysts with Visible-Light Response and Their Surface Nanostructures. *J. Am. Chem. Soc.* **2004**, *126*, 13406−13413.

(25) Ishikawa, A.; Yamada, Y.; Takata, T.; Kondo, J.; Hara, M.; Kobayashi, H.; Domen, K. Novel Synthesis and Photocatalytic Activity of Oxysulfide $Sm_2Ti_2S_2O_5$. *Chem. Mater.* **2003**, *15*, 4442−4446.

(26) Ding, J.; Sun, S.; Bao, J.; Luo, Z.; Gao, C. Synthesis of $CaIn_2O_4$ Rods and Its Photocatalytic Performance under Visible-Light Irradiation. *Catal. Lett.* **2009**, *130*, 147−153.

(27) Zhang, J.; Yu, J.; Zhang, Y.; Li, Q.; Gong, J. Noble Metal-Free Reduced Graphene Oxide-$Zn_xCd_{1-x}S$ Nanocomposite with Enhanced Solar Photocatalytic H_2-Production Performance. *Nano Lett.* **2011**, *11*, 4774−4779.

(28) Zhang, Y.; Selvaraj, R.; Sillanpaa, M.; Kim, Y.; Tai, C. Coprecipitates Synthesis of $CaIn_2O_4$ and Its Photocatalytic Degradation of Methylene Blue by Visible Light Irradiation. *Ind. Eng. Chem. Res.* **2014**, *53*, 11720−11726.

(29) Peng, S.; Li, L.; Wu, Y.; Jia, L.; Tian, L.; Srinivasan, M.; Ramakrishna, S.; Yan, Q.; Mhaisalkar, S. Size- and Shape-Controlled Synthesis of $ZnIn_2S_4$ Nanocrystals with High Photocatalytic Performance. *CrystEngComm* **2013**, *15*, 1922−1930.

(30) Chapuis, G.; Niggli, A. Crystal Structure and Crystal Chemistry of a New Sulfide $In_{6.6}Ca_{3.1}S_{13}$. *J. Solid State Chem.* **1972**, *5*, 126−130.

(31) Kato, H.; Asakura, K.; Kudo, A. Highly Efficient Water Splitting into H_2 and O_2 over Lanthanum-Doped $NaTaO_3$ Photocatalysts with High Crystallinity and Surface Nanostructure. *J. Am. Chem. Soc.* **2003**, *125*, 3082−3089.

(32) Shi, H.; Chen, G.; Zou, Z. Platinum Loaded $NaNbO_{3-x}N_x$ with Nanostep Surface Nanostructures toward Enhanced Visible-Light Photocatalytic Activity. *Appl. Catal., B* **2014**, *156−157*, 378−384.

(33) Hwang, D.; Kim, H.; Lee, J.; Kim, J.; Li, W.; Oh, S. Photocatalytic Hydrogen Production from Water over M-Doped $La_2Ti_2O_7$ (M = Cr, Fe) under Visible Light Irradiation ($\lambda > 420$ nm). *J. Phys. Chem. B* **2005**, *109*, 2093−2102.

(34) Addamo, M.; Bellardita, M.; Di Paola, A.; Palmisano, L. Preparation and Photoactivity of Nanostructured Anatase, Rutile and Brookite TiO_2 Thin Films. *Chem. Commun.* **2006**, *47*, 4943−4945.

(35) Fu, X.; Wang, X.; Chen, Z.; Zhang, Z.; Li, Z.; Leung, D.; Wu, L.; Fu, X. Photocatalytic Performance of Tetragonal and Cubic β-In_2S_3 for the Water Splitting under Visible Light Irradiation. *Appl. Catal., B* **2010**, *95*, 393−399.

(36) Kudo, A.; Omori, K.; Kato, H. A Novel Aqueous Process for Preparation of Crystal Form-Controlled and Highly Crystalline $BiVO_4$ Powder from Layered Vanadates at Room Temperature and Its Photocatalytic and Photophysical Properties. *J. Am. Chem. Soc.* **1999**, *121*, 11459−11467.

(37) Liu, S.; Yang, M.; Xu, Y. Surface Charge Promotes the Synthesis of Large, Flat Structured Graphene-(CdS Nanowire)-TiO$_2$ Nanocomposites as Versatile Visible Light Photocatalyst. *J. Mater. Chem. A* **2014**, *2*, 430−440.

(38) Yang, X.; Cui, H.; Li, Y.; Qin, J.; Zhang, R.; Tang, H. Fabrication of Ag$_3$PO$_4$-Graphene Composites with Highly Efficient and Stable Visible Light Photocatalytic Performance. *ACS Catal.* **2013**, *3*, 363−369.

(39) Ding, J.; Yan, W.; Xie, W.; Sun, S.; Bao, J.; Gao, C. Highly Efficient Photocatalytic Hydrogen Evolution of Graphene/YInO$_3$ Nanocomposites under Visible Light Irradiation. *Nanoscale* **2014**, *6*, 2299−2306.

(40) Li, Y.; Chen, G.; Zhou, C.; Sun, J. A Simple Template-Free Synthesis of Nanoporous ZnS-In$_2$S$_3$-Ag$_2$S Solid Solutions for Highly Efficient Photocatalytic H$_2$ Evolution under Visible Light. *Chem. Commun.* **2009**, *15*, 2020−2022.